

Observation of Dirac bands in artificial graphene in small-period nanopatterned GaAs quantum wells

Sheng Wang¹, Diego Scarabelli^{1,6}, Lingjie Du^{1*}, Yuliya Y. Kuznetsova², Loren N. Pfeiffer³, Ken W. West³, Geoff C. Gardner⁴, Michael J. Manfra⁴, Vittorio Pellegrini⁵, Shalom J. Wind¹ and Aron Pinczuk^{1,2}

Charge carriers in graphene behave like massless Dirac fermions (MDFs) with linear energy-momentum dispersion^{1,2}, providing a condensed-matter platform for studying quasiparticles with relativistic-like features. Artificial graphene (AG)—a structure with an artificial honeycomb lattice—exhibits novel phenomena due to the tunable interplay between topology and quasiparticle interactions^{3–6}. So far, the emergence of a Dirac band structure supporting MDFs has been observed in AG using molecular⁵, atomic^{6,7} and photonic systems^{8–10}, including those with semiconductor microcavities¹¹. Here, we report the realization of an AG that has a band structure with vanishing density of states consistent with the presence of MDFs. This observation is enabled by a very small lattice constant ($a = 50$ nm) of the nanofabricated AG patterns superimposed on a two-dimensional electron gas hosted by a high-quality GaAs quantum well. Resonant inelastic light-scattering spectra reveal low-lying transitions that are not present in the unpatterned GaAs quantum well. These excitations reveal the energy dependence of the joint density of states for AG band transitions. Fermi level tuning through the Dirac point results in a collapse of the density of states at low transition energy, suggesting the emergence of the MDF linear dispersion in the AG.

The development of semiconductor superlattice systems has stimulated great interest in the band engineering of layered semiconductors^{12–15}. Previous reports on nanopatterned artificial graphene (AG) on GaAs quantum well (QW) structures found no evidence of massless Dirac fermions (MDFs), either because of the relatively large lattice periods^{4, 16–18} or possibly because of spectral limitations¹⁹. Crucial to the observation of MDFs in semiconductor AG is the extent in the energy domain of the linearly dispersed bands around the K and K' points in the Brillouin zone (BZ)²⁰, which must overcome both thermal and disorder-induced broadenings. This condition requires AG with superior spatial uniformity, as well as lattice constants well below 100 nm. The key steps for creating the AG potential are described schematically in Fig. 1a–d. Figure 1e presents the calculated AG energy bands for a lattice constant a of 50 nm (for calculation see Supplementary Section 1). Each pillar produces an effectively attractive potential, which is approximated by a muffin-tin model (represented by a red dashed line in Fig. 1d). The energy range of the MDFs at the K and K' points in the BZ is predicted to be ~ 0.4 meV, which is considerably larger than found in previous work^{4, 16}. This extended energy range, linked to the small lattice constants, enables the experimental exploration of MDFs.

The fabricated AG lattices were superimposed on a two-dimensional electron gas confined within a 25-nm-wide one-side modulation-doped $\text{Al}_{0.1}\text{Ga}_{0.9}\text{As}/\text{GaAs}$ QW. High-resolution electron-beam lithography was used to define a honeycomb array of metallic nanodisks (Fig. 2a,b), which served as a mask for reactive-ion etching²¹. Proximity effects in GaAs are especially significant²² and required consideration during electron-beam lithography, for example, through the optimization of exposure and development conditions (see Methods). Honeycomb arrays of metal disks with lattice constants between 40 nm (Supplementary Fig. 2a) and 70 nm were fabricated extending over an area of $200 \times 200 \mu\text{m}^2$. The disk radius was optimized using the calculation described in Supplementary Fig. 1. The fabricated masks displayed excellent short-range uniformity and long-range order, essential requirements for the observation of Dirac fermion physics. Inductively coupled plasma reactive-ion etching was used to create honeycomb lattices of pillars in the substrate, as illustrated in Fig. 2c,d (see Methods). This procedure allowed us to obtain an AG lattice with a nearly vertical pillar profile, as presented in Supplementary Fig. 2b. Precise control of the etch depth enabled tuning of the magnitude of the AG potential and of the Fermi energy. AG samples with different lattice constants were studied, as listed in Supplementary Table 1. Here, we present the results from two patterns with $a = 50$ nm. Sample A was created with an etching depth of 70 nm (Fig. 2b,d), and sample B had an etching depth of 75 nm. This facilitated the in-depth study of the AG band structure and monitoring of the emergence of MDF states.

Resonant inelastic light scattering (RILS) has been demonstrated to be an effective probe of electron states in AG¹⁹, but the low-lying states near the Dirac cones have not been accessed until the present work. Here, we report results based on photoluminescence (Supplementary Figs. 3 and 4) and RILS methods (Supplementary Fig. 5). RILS measurements of low-energy excitations at low temperature (4 K) are shown in Fig. 3a for sample A. The RILS signal overlaps with weak photoluminescence, which is subtracted, as shown in Fig. 3b. Typical spectra after removal of the photoluminescence are shown in Fig. 3c, in which a clearly identifiable narrow peak (full-width at half-maximum (FWHM) of ~ 0.21 meV) near 0.85 meV is labelled E_L . A weaker broader peak located near 1.3 meV is labelled E_H . These RILS spectra are interpreted as arising from transitions between states belonging to different AG energy bands, specifically from the c_{01} band to the c_{02} band, as indicated in Fig. 3d. Moreover, by tuning the etching depth, the Fermi energy can be reduced to a lower value, enabling the observation of transitions from c_{00} to c_{01} . RILS measurements in this regime provide a direct observation of the AG band structure, as explained in the discussion for sample B.

¹Department of Applied Physics and Applied Mathematics, Columbia University, New York, NY, USA. ²Department of Physics, Columbia University, New York, NY, USA. ³Department of Electrical Engineering, Princeton University, Princeton, NJ, USA. ⁴Department of Physics and Astronomy, and School of Materials Engineering, and School of Electrical and Computer Engineering, Purdue University, West Lafayette, IN, USA. ⁵Istituto Italiano di Tecnologia, Graphene Labs, Genova, Italy. Present address: ⁶Rigetti Quantum Computing, Berkeley, CA, USA. *e-mail: ld2751@columbia.edu

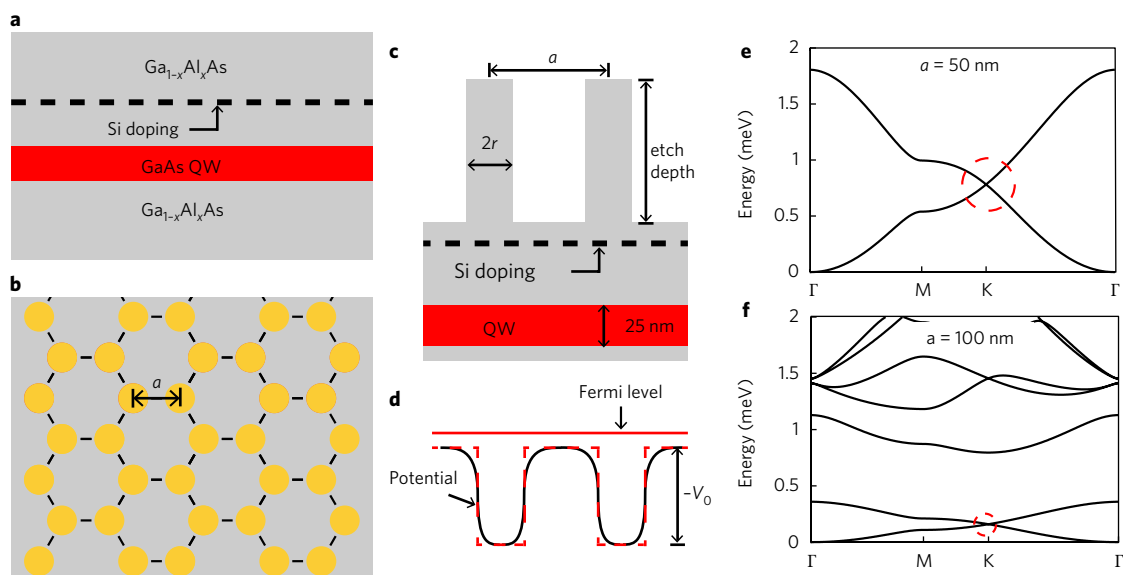


Fig. 1 | Principle of the realization of AG in a modulation-doped $\text{Al}_{1-x}\text{Ga}_x\text{As}/\text{GaAs}$ QW. **a**, Schematic of the layer sequence in the QW sample. The QW is positioned 110 nm below the surface and 30 nm below the Si δ -doping layer. The as-grown electron density is $1.8 \times 10^{11} \text{ cm}^{-2}$, with a Fermi energy of 6.3 meV and low-temperature mobility of $3.2 \times 10^6 \text{ cm}^2 \text{ V}^{-1} \text{ s}^{-1}$. **b**, Schematic of an etch-mask with honeycomb topology with lattice constant a . **c**, Illustration of the sample profile after etching, showing the parameters that define the AG pattern. r is the radius of the pillar. **d**, Schematic of the periodic potential induced by the AG pattern (black solid line). $-V_0$ is the potential depth in the etched area. In the evaluation of the AG band structure, we used a honeycomb muffin-tin potential (red dashed line) within the single-particle approximation and solved Schrödinger's equation with a basis of plane waves (Supplementary Section 1). **e**, Lowest two AG bands for typical parameters $a = 50 \text{ nm}$, $V_0 = -10 \text{ meV}$ and $r = 8.5 \text{ nm}$. **f**, AG band structure for $a = 100 \text{ nm}$, $V_0 = -2 \text{ meV}$ and $r = 17 \text{ nm}$. In **e** and **f**, the linear dispersion range is shown (highlighted by the dashed circle) to be increased by a factor of ~ 4 for $a = 50 \text{ nm}$.

RILS spectra of the inter-AG-band transitions are expected to be proportional to the joint density of states (JDOS) for vertical transitions (no wavevector change), as described in Supplementary Section 4. The calculated JDOS peak shown in Fig. 3c, which very precisely overlaps peak E_L , is largely due to transitions in the regions of wavevector space marked as 1 and 2 in Fig. 3c,d. This agreement indicates that disorder-induced broadening plays a minor role, a crucial condition for the appearance of MDFs. In region 1, the c_{01} and c_{02} bands are nearly parallel, which results in a maximum in the JDOS. Transitions in region 2 of the JDOS are at the Dirac cones formed at the K and K' points. Transitions in region 3 are mainly transitions around the M point in the BZ where the c_{01} and c_{02} bands have fairly different k -dispersion, generating a broader peak E_H . The excellent agreement between the RILS spectra and the calculated JDOS is strong evidence of the energy dispersion of the AG bands formed under the periodic potential generated by the fabricated nanopatterns.

Transitions from region 2 are of particular interest because they originate from the segments of the reciprocal lattice BZ near the K and K' points, where MDFs are formed. To gain further insight into the contribution from transitions within this region to the E_L peak, we take advantage of the resonance enhancement of RILS, shown in Fig. 4. At lower incident photon energies, the asymmetric E_L peak is dominant, as seen in the upper spectrum in Fig. 4a. Region 2 transitions occur at the high-energy cutoff of the E_L peak (Fig. 4a). At this lower incident photon energy, the E_L peak mainly results from the resonantly enhanced transitions around the Dirac points, as shown in the inset to Fig. 4b. The low-energy tail of the E_L peak (grey area) probably arises from non-vertical transitions due to the impact of residual disorder, as indicated in the inset to Fig. 4a and discussed in Supplementary Section 4. The sharp cutoff of the E_L peak at high energy is interpreted as the cutoff of the JDOS due to Dirac cones at the K and K' points. These results support the existence of well-defined MDFs.

A key picture of the electron states near the Dirac points can be obtained from inter-AG-band transitions measured in an AG structure in which the Fermi level lies below the energy at the K and K' points. This is achieved in our system by suitably tuning the depth of etching during fabrication of the AG lattices. Figure 5a

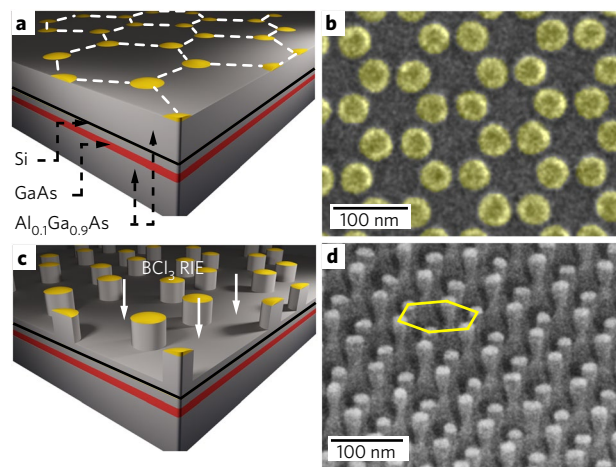


Fig. 2 | Nanofabrication of AG pattern on a modulation-doped $\text{Al}_{0.1}\text{Ga}_{0.9}\text{As}/\text{GaAs}$ QW sample. **a**, Illustration of the etch-mask consisting of an array of metal nanodisks arranged in a honeycomb lattice on the surface of a QW sample. **b**, SEM micrograph of the mask of gold nanodisks with 50 nm lattice constant (false colour). **c**, Cartoon representing the AG nanopattern obtained by anisotropic dry etching through the mask using a BCl_3 -based gas mixture. **d**, SEM image of an AG lattice with a lattice constant of 50 nm after the ICP-RIE dry etch and removal of the gold mask. The etch depth is 70 nm.

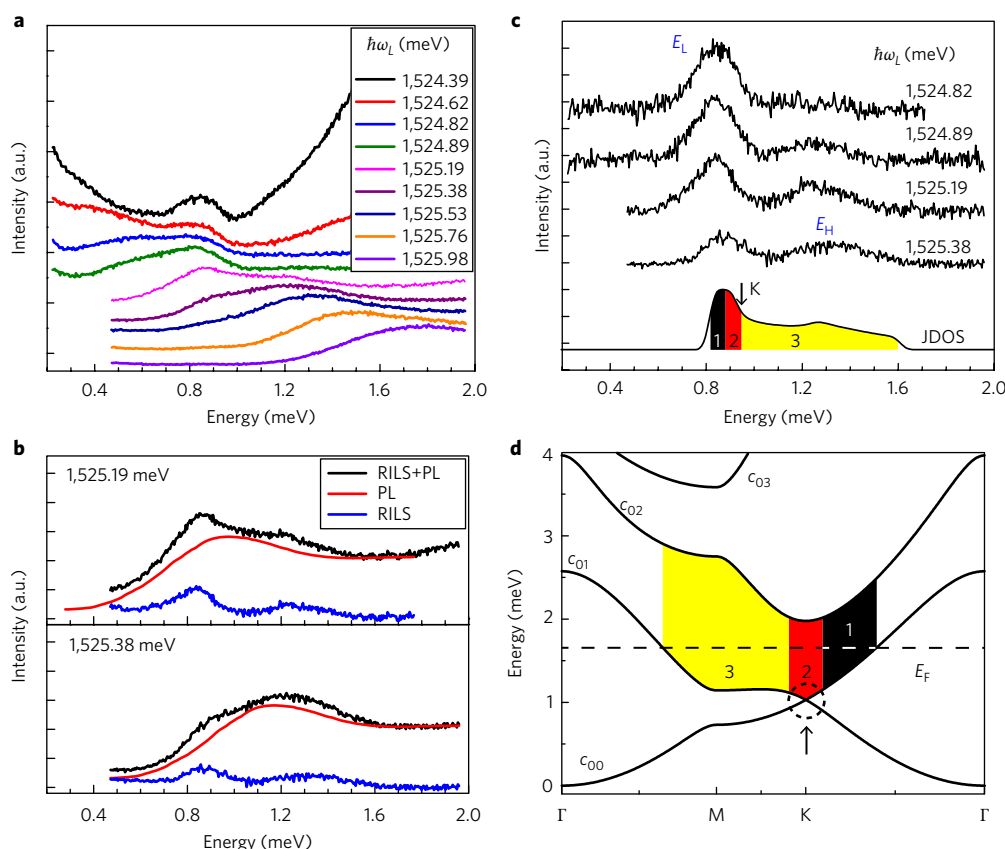


Fig. 3 | Spectra of inter-AG-band transitions in sample A. **a**, Spectra of low-lying excitations at different incident photon energies $\hbar\omega_L$. The RILS signal overlaps with the photoluminescence background. **b**, Subtraction of the background photoluminescence (red) reveals the RILS signal (blue). **c**, RILS spectra for different incident photon energies $\hbar\omega_L$ after removal of the photoluminescence background. Two peaks are identified at $E_L = 0.85$ meV and $E_H = 1.3$ meV. The calculated JDOS of the inter-AG-band transitions between the c_{01} and c_{02} bands is in agreement with the observed spectra. The different contributions to the JDOS are explained in **d**. **d**, Illustration of the electronic transitions associated with the observed RILS spectra. The AG bands are calculated with $a = 50$ nm, $r = 8.5$ nm and $V_0 = -6.4$ meV. The Fermi energy E_F used in the calculation of the JDOS is 1.7 meV (Supplementary Section 3). The linear dispersion range in c_{00} and c_{01} bands is highlighted by a dashed circle. Three regions of the reciprocal space are identified with different colours in **d** and the transitions in each region are related to the corresponding energy range of the JDOS in **c**.

presents spectra from sample B, an AG lattice device with $a = 50$ nm and etching depth of 75 nm, resulting in a lower Fermi energy than that in sample A. RILS spectra are shown in Fig. 5b after subtracting a photoluminescence background signal (Supplementary Fig. 6). The lowering of the Fermi energy results in strikingly different RILS spectra from those in sample A, as seen in the upper panel of Fig. 5c. At $\hbar\omega_L = 1,525.75$ meV, no peak is observed. When $\hbar\omega_L$ is decreased to 1,525.2 meV, a weak RILS peak is seen near 1 meV, which becomes stronger for lower $\hbar\omega_L$ and its energy decreases. When $\hbar\omega_L$ is below 1,525.2 meV, a strong RILS peak is observed near an energy of 0.5 meV. This RILS peak reaches its maximum intensity at $\hbar\omega_L = 1,525.0$ meV due to the maximum in resonance enhancement.

The spectra of low-energy transitions seen in Fig. 5b,c are remarkably different from those in Fig. 3a, where a strong RILS peak is centred at 0.8 meV. This crucial difference between samples A and B is due to the lower Fermi energy—0.9 meV in sample B as opposed to 1.7 meV in sample A—so c_{00} is the only AG band that is populated in sample B and $c_{00} \rightarrow c_{01}$ are the lowest inter-AG-band transitions. The calculated AG band structure in Fig. 5d showing flat bands near the M point and a linear dispersion near the Dirac point is characteristic of AG. These features of AG are clearly manifested in the RILS spectra shown in Fig. 5c. The intensity maximum at 0.5 meV in the spectrum obtained with $\hbar\omega_L = 1,525$ meV is

interpreted by the large JDOS for the $c_{00} \rightarrow c_{01}$ transitions shown in red in the lower panel of Fig. 5c and in Fig. 5d. The higher energy transitions seen in the spectrum obtained with $\hbar\omega_L = 1,525.37$ meV arise mostly from transitions in the yellow region in the lower panel of Fig. 5c and in Fig. 5d.

We highlight the rapid collapse of the RILS intensity in the very low energy limit (approaching 0.1 meV) in Fig. 5c. This experimental observation corresponds to the collapse of the JDOS for the $c_{00} \rightarrow c_{01}$ transitions near the Dirac point, as seen in the lower panel of Fig. 5c and in Fig. 5d (black curve), which follows directly from the vanishing DOS of the linearly dispersing Dirac bands (Supplementary Figs. 7 and 8). These results can thus be regarded as a consequence of Dirac cones at the K and K' points in the BZ of the honeycomb lattice of AG.

To summarize, we have realized artificial graphene in a modulation-doped AlGaAs/GaAs QW patterned with two-dimensional honeycomb lattices with very small period, excellent long-range order, short-range uniformity and anisotropic etching profile. RILS spectra reveal transitions of electrons between AG bands with vanishing DOS, as expected for well-defined MDFs near the K(K') points. The presence of MDFs over a macroscopic region of a nanofabricated semiconductor system opens new research opportunities. The small-period AG lattices in semiconductors, suitable for device stability and integration, constitute a tunable platform for quantum

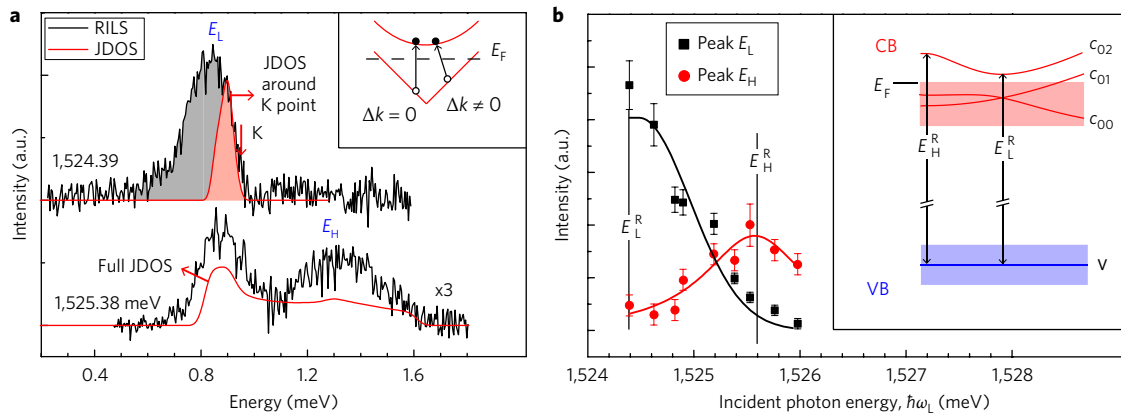


Fig. 4 | Dependence of RILS on incident photon energy in sample A. a, RILS spectra at two different incident photon energies $\hbar\omega_L$ as labelled (in meV). Inset: vertical ($\Delta k = 0$) and non-vertical ($\Delta k \neq 0$) transitions between the c_{01} and c_{02} AG bands (for more details see Supplementary Section 4). The upper spectrum, taken at $\hbar\omega_L = E_L^R$ (see inset to **b**) is largely derived from transitions close to the K and K' points. It shows an asymmetric E_L peak with a sharp cutoff on the high-energy side. The contribution to the JDOS from transitions near the K and K' points (red curve) accurately describes the line shape of the high-energy cutoff due to the vanishing DOS at the Dirac point. The signal at lower energy (grey area) is explained by non-vertical transitions due to residual disorder (see inset). The lower spectrum, taken at higher $\hbar\omega_L$ and showing peaks at E_L and E_H , is interpreted with the JDOS (in red) with contributions from a larger range of k space (regions 1, 2 and 3 in Fig. 3c,d). **b**, Integrated intensities of the E_L and E_H peaks as a function of $\hbar\omega_L$ showing maxima at E_L^R and E_H^R . Vertical bars are estimates of uncertainty in the quantitative determinations of integrated intensities. Inset: band diagram (not to scale) showing transitions from the valence band (VB) to the conduction band (CB) of the AG potential, which explains the observed resonant enhancement maxima at E_L^R and E_H^R .

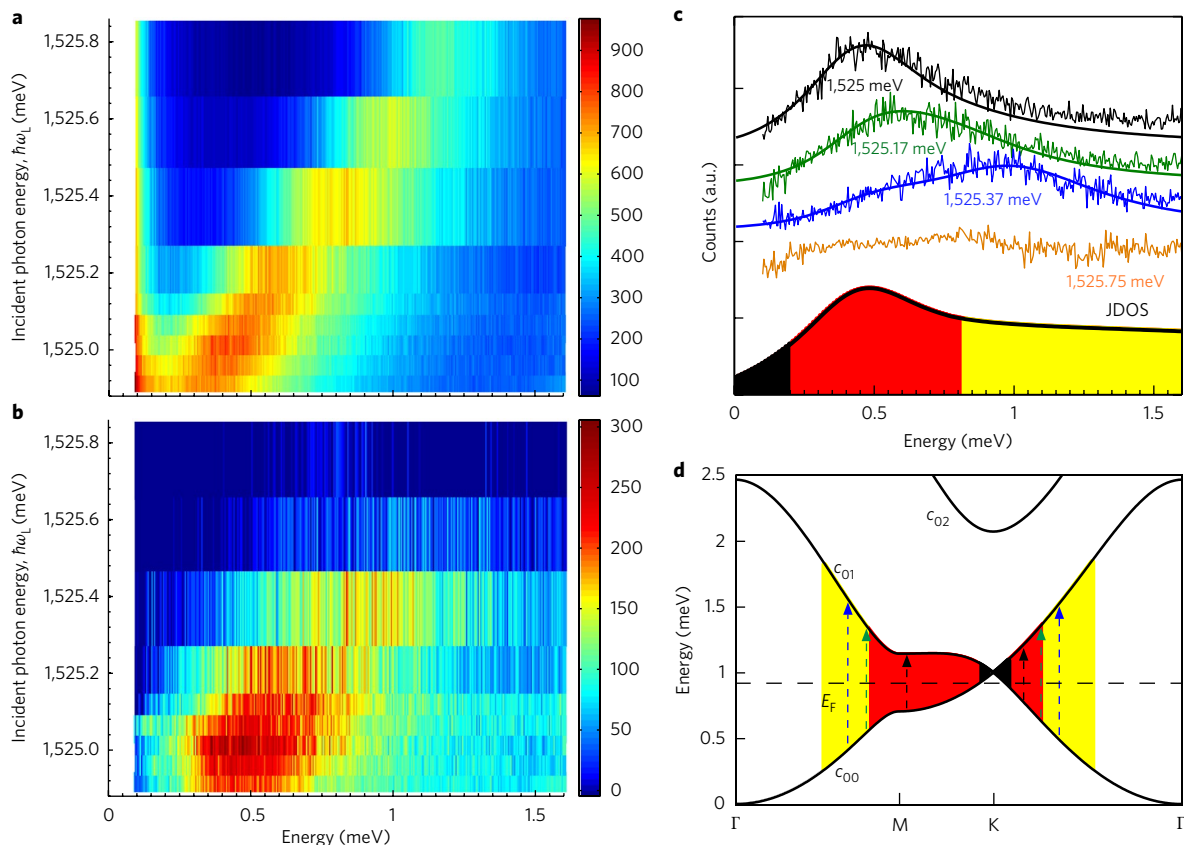


Fig. 5 | Spectra of inter-AG-band transitions in sample B with a smaller Fermi energy than that in sample A. a, Colour plot of RILS spectra for incident laser photon energy $\hbar\omega_L$ measured at $T = 4.2$ K. The colour bar indicates intensity. **b**, Colour plot of spectra after removal of a photoluminescence background to reveal RILS intensities of low-lying excitations. **c**, Bottom: JDOS calculated for transitions between c_{00} and c_{01} states. The JDOS is broadened by Gaussian disorder of width 0.3 meV. Top: RILS spectra after removal of the photoluminescence background. Values of $\hbar\omega_L$ are indicated. Solid lines are calculated RILS intensities that include the JDOS in the lower panel modified by resonance enhancement. The lower energy limit accessible in these RILS spectra is 0.1 meV due to the finite width of the laser line. **d**, Calculated AG band structure illustrating the electronic transitions associated with the observed RILS spectra. The AG bands were calculated with $a = 50$ nm, dot radius $r = 8.5$ nm, $V_0 = -6.9$ meV, $T = 4.2$ K and $E_F = 0.9$ meV. Due to the thermal population, transitions highlighted by black are allowed. The Fermi level is indicated with a dashed line. In the bottom panel of **c** and in **d**, three distinct regions for the $c_{00} \rightarrow c_{01}$ inter-AG transitions are identified by different colours.

simulators of the novel quantum regime of MDFs not attainable in natural graphene. The implementation of AG lattices in materials with strong spin–orbit coupling should enable the exploration of topological insulating states^{23–25}. The tunable parameters also make AG lattices a realm for investigations of fractal quantum physics^{26–28}, the control of spin–orbit coupling^{29, 30} and simulation of the opening of an energy gap by breaking inversion symmetry. Moreover, through suitable state-of-the-art nanofabrication we can create defects such as quantum dots in the lattice to study tunnelling effects involving MDFs.

Methods

Methods, including statements of data availability and any associated accession codes and references, are available at <https://doi.org/10.1038/s41565-017-0006-x>.

Received: 19 June 2015; Accepted: 21 September 2017;

Published online: 27 November 2017

References

- Novoselov, K. S. et al. Two-dimensional gas of massless Dirac fermions in graphene. *Nature* **438**, 197–200 (2005).
- Zhang, Y. B., Tan, Y. W., Stormer, H. L. & Kim, P. Experimental observation of the quantum Hall effect and Berry's phase in graphene. *Nature* **438**, 201–204 (2005).
- Park, C. H. & Louie, S. G. Making massless Dirac fermions from a patterned two-dimensional electron gas. *Nano Lett.* **9**, 1793–1797 (2009).
- Gibertini, M. et al. Engineering artificial graphene in a two-dimensional electron gas. *Phys. Rev. B* **79**, 241406 (2009).
- Gomes, K. K., Mar, W., Ko, W., Guinea, F. & Manoharan, H. C. Designer Dirac fermions and topological phases in molecular graphene. *Nature* **483**, 306–310 (2012).
- Tarruell, L., Greif, D., Uehlinger, T., Jotzu, G. & Esslinger, T. Creating, moving and merging Dirac points with a Fermi gas in a tunable honeycomb lattice. *Nature* **483**, 302–305 (2012).
- Graß, T., Chhajlany, R., Tarruell, L., Pellegrini, V. & Lewenstein, M. Proximity effects in cold atom artificial graphene. *2D Mater.* **4**, 015039 (2017).
- Sepkhanov, R. A., Bazally, Ya. B. & Beenakker, C. W. Extremal transmission at the Dirac point of a photonic band structure. *Phys. Rev. A* **75**, 063813 (2007).
- Haldane, F. D. M. & Raghu, S. Possible realization of directional optical waveguides in photonic crystals with broken time-reversal symmetry. *Phys. Rev. Lett.* **100**, 013904 (2008).
- Ling, L., Joannopoulos, J. D. & Soljacic, M. Topological photonics. *Nat. Photon.* **8**, 821–829 (2014).
- Jacqmin, T. et al. Direct observation of Dirac cones and a flatband in a honeycomb lattice for polaritons. *Phys. Rev. Lett.* **112**, 116402 (2014).
- Heitmann, D. & Kotthaus, J. The spectroscopy of quantum dot arrays. *Phys. Today* **46**, 56–63 (1993).
- Hirler, F. et al. Spatially direct and indirect optical transitions in shallow etched GaAs/AlGaAs wires, dots and antidots. *Semicond. Sci. Technol.* **8**, 617–621 (1993).
- Weiner, J. S. et al. Electron gas in semiconductor multiple quantum wires: spatially indirect optical transitions. *Phys. Rev. Lett.* **63**, 1641–1644 (1989).
- Egeler, T. et al. Anisotropic plasmon dispersion in a lateral quantum-wire superlattice. *Phys. Rev. Lett.* **65**, 1804–1807 (1990).
- Singha, A. et al. Two-dimensional Mott–Hubbard electrons in an artificial honeycomb lattice. *Science* **332**, 1176–1179 (2011).
- Soibel, A., Meirav, U., Mahalu, D. & Shtrikman, H. Fabrication and transport measurements of honeycomb surface superlattices. *Semicond. Sci. Technol.* **11**, 1756–1760 (1996).
- Nadvornik, L. et al. From laterally modulated two-dimensional electron gas towards artificial graphene. *New J. Phys.* **14**, 053002 (2012).
- Wang, S. et al. Observation of electron states of small period artificial graphene in nano-patterned GaAs quantum wells. *Appl. Phys. Lett.* **109**, 113101 (2016).
- Polini, M., Guinea, F., Lewenstein, M., Manoharan, H. C. & Pellegrini, V. Artificial honeycomb lattices for electrons, atoms and photons. *Nat. Nanotech.* **8**, 625–633 (2013).
- Scarabelli, D. et al. Fabrication of artificial graphene in a GaAs quantum heterostructure. *J. Vac. Sci. Technol. B* **33**, 06FG03 (2015).
- Czaplewski, D. A., Holt, M. V. & Ocola, L. E. The range and intensity of backscattered electrons for use in the creation of high fidelity electron beam lithography patterns. *Nanotechnology* **24**, 305302 (2013).
- Qi, X. L. & Zhang, S. C. Topological insulators and superconductors. *Rev. Mod. Phys.* **83**, 1057–1110 (2010).
- Hasan, M. Z. & Kane, C. L. Topological insulators. *Rev. Mod. Phys.* **82**, 3045–3067 (2010).
- Sushkov, O. P. & Neto, A. H. C. Topological insulating states in laterally patterned ordinary semiconductors. *Phys. Rev. Lett.* **110**, 186601 (2013).
- Albrecht, C. et al. Evidence of Hofstadter's fractal energy spectrum in the quantized Hall conductance. *Phys. Rev. Lett.* **86**, 147–150 (2001).
- Geisler, M. et al. Detection of a Landau band-coupling-induced rearrangement of the Hofstadter butterfly. *Phys. Rev. Lett.* **92**, 256801 (2004).
- Melinte, S. et al. Laterally modulated 2D electron system in the extreme quantum limit. *Phys. Rev. Lett.* **92**, 036802 (2004).
- Žutić, I., Fabian, J. & Sarma, S. Spintronics: fundamentals and applications. *Rev. Mod. Phys.* **76**, 323–410 (2004).
- Han, W., Kawakami, R., Gmitra, M. & Fabian, J. Graphene spintronics. *Nat. Nanotech.* **9**, 794–807 (2014).

Acknowledgements

The work at Columbia University was supported by grant DE-SC0010695 from the US Department of Energy Office of Science, Division of Materials Sciences and Engineering, and by the National Science Foundation, Division of Materials Research, under award DMR-1306976. The growth of GaAs/AlGaAs QWs at Purdue University was supported by grant DE-SC0006671 from the US Department of Energy Office of Science, Division of Materials Sciences and Engineering. The growth of GaAs/AlGaAs QWs at Princeton University was supported by the Gordon and Betty Moore Foundation under award GMBF-2719 and by the National Science Foundation, Division of Materials Research, under award DMR-0819860. V.P. acknowledges the European Graphene Flagship (contract no. CNECT-ICT-604391) for financial support and the Italian Ministry of Research (MIUR) through the program 'Progetti Premiali 2012' – Project 'ABNANOTECH'. The authors thank G.P. Watson for technical assistance with the ICP-RIE etching and A. Levy and F. Qiao for discussions.

Author contributions

S.W. performed ICP-RIE processing and optical experiments. S.W. and L.D. performed numerical calculations. S.W., L.D., Y.Y.K. and A.P. analysed the data. D.S. and S.W. fabricated the AG lattices. G.C.G., M.J.M., K.W. and L.N.P. fabricated the QW samples. S.W., D.S., L.D., Y.Y.K., S.J.W. and A.P. co-wrote the paper with input from other authors. V.P., S.J.W. and A.P. conceived the experiments and supervised the project.

Competing interests

The authors declare no competing financial interests.

Additional information

Supplementary information is available for this paper at <https://doi.org/10.1038/s41565-017-0006-x>

Reprints and permissions information is available at www.nature.com/reprints.

Correspondence and requests for materials should be addressed to L.D.

Publisher's note: Springer Nature remains neutral with regard to jurisdictional claims in published maps and institutional affiliations.

Methods

Fabrication of the AG nanopattern. Electron-beam lithography at 80 kV and a beam current of 400 pA (e-beam writer nB4, NanoBeam) was used to pattern $200 \times 200 \mu\text{m}^2$ honeycomb arrays of circles of various pitch, diameter and exposure dose. We used a double-layer resist stack of poly(methylmethacrylate) (PMMA) with different molecular weights to facilitate metal liftoff by forming an undercut profile, which was developed in a solution of methyl-isobutyl ketone:isopropanol (MIBK:IPA, 1:3). An Angstrom EvoVac electron-beam evaporator was used to deposit 2 nm Ti (adhesion layer) and 8 nm Au. After metal liftoff, the mask-carrying samples were examined using a Hitachi S-4700 scanning electron microscope. A Samco International RIE200iP was used to perform the inductively-coupled plasma reactive-ion etching. The gas used was a mixture of 50 s.c.c.m. Ar and 5 s.c.c.m. BCl_3 , which has been shown to etch AlGaAs/GaAs heterostructures with high anisotropy²¹. For the presented patterns, the etching time was 110 s. The etch recipe was optimized

to achieve a high degree of physical bombardment and reduced chemical etching. For details regarding the fabrication procedure and optimization see ref. ²¹.

Optical measurements. The sample was mounted in an optical cryostat with a base temperature of 4 K. The RILS measurements were performed in a back-scattering configuration, with the incident laser beam almost perpendicular (within 6°) to the sample (Supplementary Section 4). A tunable Ti:sapphire laser with spot diameter of $\sim 100 \mu\text{m}$ and typical power of $\sim 1 \text{ mW}$ was focused on the AG nanopattern. Spectra were collected using a liquid-nitrogen-cooled charge-coupled device through a double-grating spectrometer (Spex 1404).

Data availability. The data that support the plots within this paper and other findings of this study are available from the corresponding author upon reasonable request.